Nuclear Science and Techniques (2026) 37:39
https://doi.org/10.1007/s41365-025-01867-1

Experimental investigation on trigger dynamics of molten droplet under external disturbance pressure during fuel-coolant interaction

He-Lin Chen[1] · Cheng Peng[1] · Xian-Pin Meng[1] · Jian Deng[2] · Jiang Wu[1]

Received: 19 July 2024 / Revised: 16 October 2024 / Accepted: 10 November 2024 / Published online: 9 January 2026

Abstract

Fuel-coolant interaction (FCI) remains one of the most complex challenges in severe accident research, with the triggering process being a key aspect that may govern subsequent fine fragmentation and potential steam explosions. In this study, the evolution characteristics of droplet-water interactions under external disturbance conditions were investigated using a self-designed FCI experimental setup. The experimental observations revealed that cavity formation reduced the drag force on the droplet, thereby increasing its peak velocity. However, the external disturbance pressure can disrupt the cavity, leading to a reduction in the droplet peak velocity. Furthermore, it was found that an increase in external disturbance pressure tended to increase the peak value of the droplet expansion rate, thereby promoting the fine-fragmentation process. This effect holds regardless of the initial droplet temperature, coolant temperature, or even when using droplet materials such as lead, which is generally considered unfavorable for steam explosions. Comparative analyses indicated that a higher external disturbance pressure may shorten the triggering time of the droplet surface and enhance the trigger intensity. These findings provide important phenomenological insights for further investigation of the triggering mechanisms in the initial stage of fuel-coolant interactions.

Keywords External disturbance pressure · Molten droplet · Transit velocity · Expansion rate · Fuel-coolant interaction

1 Introduction

In the event of a severe accident at a nuclear power plant, the loss of coolant may prevent the core from being adequately cooled, potentially leading to a core meltdown. If the high-temperature core material subsequently comes into direct contact with a low-temperature coolant, a steam explosion may occur. Zhong et al. [1] simulated the pressure load generated by an ex-vessel steam explosion in a PWR cavity, showing that in the worst-case scenario, the pressure load can exceed the design capacity of a typical reactor cavity wall. The resulting shock wave can compromise the structural integrity of the reactor and release radioactive materials into the environment, posing serious safety risks to nuclear power plants and personnel [2–5]. This phenomenon, known as fuel-coolant interaction (FCI), and its potential consequences have drawn significant attention from researchers in the field of nuclear safety [6–10]. FCI is relevant not only for light water reactors but also for sodium- and lead-cooled fast reactors, where understanding its progression is essential for the design and licensing of Generation IV reactor concepts [11]. For instance, in the case of an unprotected loss of flow or transient overpower accident in such reactors, a core disruptive accident (CDA) could cause fuel relocation and the ejection of molten corium into a volatile coolant pool [12]. During this process, the corium may undergo extensive fragmentation owing to thermal and hydrodynamic

This work was supported by the operating fund of Key Laboratory of Nuclear Power Systems and Equipment (Shanghai Jiao Tong University), Ministry of Education, China, the Natural Science Foundation of Shanghai Municipality (25ZR1402177), and the National Natural Science Foundation of China (12105167).

✉ Cheng Peng
diomio@shiep.edu.cn

✉ Jian Deng
dengjian_npic@163.com

[1] College of Energy and Mechanical Engineering, Shanghai University of Electric Power, Shanghai 200090, China

[2] Science and Technology on Reactor System Design Technology Laboratory, Nuclear Power Institute of China, Chengdu 610213, China

instabilities [13, 14] a behavior that differs from the FCI in water-cooled reactors owing to differences in thermal and fluid properties. Moreover, in certain designs, such as an annular fuel configuration for a lead fast reactor, fuel pin failure could trigger interactions between high-momentum jets, containing ejected fuel in the form of solid grains or molten droplets, and metallic coolant droplets. The outcomes of such interactions are associated with reactor safety issues, known as pin failure propagation [15]. Therefore, it is essential to understand the mechanisms and characteristics of each stage of the FCI to prevent steam explosions.

The FCI process can be broadly divided into four key stages [16, 17]: pre-mixing, triggering, propagation, and expansion stages. Over the past few decades, Li et al. [18] observed that the molten material temperature significantly affects the vapor explosion behavior and pressure through experiments and that increasing the coolant temperature reduces the vapor explosion pressure—a finding later corroborated by Huang et al. [19]. Furthermore, based on experiments involving low-temperature molten tin alloy droplets entering water, Li et al. [20] proposed a physical mechanism in which the coolant trapped inside the molten material may be heated and vaporized, leading to a vapor explosion; however, this phenomenon is not observable through visualization methods. Regarding the pre-mixing stage, Li et al. [21] studied the settling behavior of high-temperature particles in a coolant liquid. They concluded that film boiling on the particle surface slows the particle settling speed as either the particle or coolant temperature increases, which may significantly influence the subsequent triggering process. Rather than focusing on hydrodynamic effects, Lin and Cao [22] analyzed the MIXA experiment using simulation codes and recommended the use of a thermal fragmentation model for high-temperature molten droplets under low Weber number conditions. In recent years, it has been seen that numerous FCI-related studies aimed at understanding fragmentation mechanisms, steam explosion potential, and debris bed characteristics in light water-cooled reactors and liquid metal-cooled fast reactors were conducted. Johnson et al. [12] investigated interactions between metallic corium jets and sodium at the MELT facility. Both X-ray imaging and debris analysis indicated that crust formation induced spontaneous thermal fragmentation. Rao et al. [14] studied the fragmentation of simulated corium in sodium using real-time X-ray imaging and concluded that the potential for energetic interaction is lower in sodium than in water. Xiang et al. [5] focused on debris bed characteristics resulting from fuel-coolant interactions and analyzed the effects of jet breakup and droplet fragmentation for various simulant materials. Cheng et al. [23] conducted coolant-injection (CI) experiments comparing the outcomes of delivering water into Bi-Sn-In alloy and lead-bismuth eutectic (LBE) alloy, contributing to the understanding of CDAs in sodium-cooled fast reactors. Choi et al. [24] performed numerical simulations of jet breakup by adopting an improved surface tension model in two typical configurations; and verified that the SPH simulation results were consistent with the experimental results. These findings offer valuable insights and suggest a possible relationship between droplet motion and steam explosions.

The triggering stage plays a critical role in determining the probability and severity of steam explosions. After passing through the pre-mixing stage, the high-temperature melt forms droplets of various sizes, each enveloped by a stable vapor film owing to heat exchange with the coolant. At this point, internal or external disturbances can cause the vapor film to collapse, leading to a local high pressure and triggering [25–27]. Internal disturbances, known as self-triggering, can result from the cooling of the melt itself. When the melt temperature drops below the film boiling temperature, the vapor film stability is compromised, leading to triggering [28]. External triggering arises from factors such as ambient pressure changes, melt-melt collisions, coolant convection, and entrainment. Such disturbances force the coolant into contact with the melt, initiating the trigger [29]. Therefore, understanding vapor film collapse is essential for studying the triggering of steam explosions [30].

To elucidate the mechanisms of the triggering stage, researchers have conducted extensive experimental studies. Early studies focused primarily on melt triggering in the absence of external disturbances. Dullforce [31] performed numerous experiments on single tin droplet-water interactions and compiled trigger strength data across different droplet and water temperatures, leading to the development of a temperature interaction zone (TIZ) for tin and water. Within the TIZ, steam explosions occur spontaneously when tin droplets enter the water, and the TIZ boundaries are strongly influenced by the physical properties and mass of the droplets. Kouraytem [32] investigated interactions between Field's metal droplets and cooling water at varying initial temperatures, finding that the lower threshold temperature for steam explosion was approximately 400 °C. Rayleigh-Taylor instability was identified as the main cause of vapor-liquid interface instability, with its wavelength decreasing as the steam explosion intensity increased. Watts [33] conducted single-droplet experiments using tin, gallium, and bismuth, focusing on vapor film collapse and the subsequent droplet fragmentation. The results indicated that materials with low surface tension and density experienced significantly intensified vapor explosions. Meanwhile, Corradini [34] analyzed FCI experiments performed by Nelson [35] at Sandia National Laboratories and concluded that: (1) higher water temperatures stabilize the vapor film, thereby suppressing triggering; (2) non-condensable gases, such as hydrogen, in the vapor film can inhibit self-triggering in some droplets; and (3) external triggers can induce

steam explosions in droplets that do not self-trigger. To further clarify the melt triggering mechanisms, researchers have performed vapor film rupture experiments under externally applied disturbances. Bankoff [36] studied vapor film collapse of Freon and ethanol on an electrically heated nickel tube using a pressure step method, with step magnitudes of 0.1–0.5 MPa and pulse rise times ranging from 80 μs to 344 ms. They found that vapor film rupture may occur when the pressure step exceeds three times the ambient pressure and the pulse rise time is less than 150 ms. Inoue [37] conducted vapor film rupture experiments on an electrically heated platinum foil, using the pressure step method with magnitudes of 0.1–0.5 MPa and rise times of 0.1–7.5 ms. Partial vapor film collapse was observed at pressure steps of approximately 0.5 MPa, with the extent of collapse increasing as the pulse rise time decreased. Naylor and Patrick [38] conducted a series of vapor film rupture experiments using a hemispherical brass rod at 770 K immersed in a liquid pool and studied both self-triggered and externally triggered conditions. Their results indicated that vapor film collapse occurs when the sum of the melt surface roughness and the amplitude of the vapor-liquid interface wave exceeds the average vapor film thickness. Recent experimental analyses of FCI have been conducted by several research groups. For specific details, refer to Table 1.

Regarding small-scale experiments involving external pressure disturbances, previous studies have shown that different geometries and pressure dynamics significantly influence vapor film rupture under constant temperature conditions. However, the mechanism of external triggering of droplet-shaped melts under high-temperature conditions remains unclear. To better understand this issue, further investigations into the evolution characteristics of the melt during the triggering stage are necessary.

In this study, a small-scale experimental facility was established to investigate the interactions between high-temperature melts and low-temperature coolants using a visualization approach. The setup was designed to support FCI research under externally applied disturbances. By analyzing and comparing the characteristic melt-water interaction phenomena, this study quantified the variations in the transient melt velocity, expansion rate, triggering pressure peaks, and fragment morphology under various conditions. These findings provide deeper insights into the triggering mechanisms of molten droplets during FCI.

2 Experimental preparations

2.1 Experimental facility

The experimental facility used in this study is illustrated in Fig. 1, was designed with reference to previous experimental setups [39–41] and adapted to meet the specific objectives and technical requirements of the present research. The system consists of the following major components: a vacuum graphite electrode furnace, a melt-release mechanism, a transparent water tank, temperature and pressure acquisition instruments, a high-speed camera, and an external disturbance device.

The vacuum graphite electrode furnace features a double-layer annular structure heated by five graphite electrodes [42], with a maximum design temperature of 2200 °C. A graphite crucible placed inside the furnace is used to melt the metal, and the temperature at the center of the heating zone is monitored using an infrared pyrometer. The exterior of the furnace is lined with graphite wool insulation to minimize heat loss. In addition, a vacuum system was employed to prevent the oxidation of the graphite electrodes and molten material.

The melt-release device consists of a graphite support rod and an electric lift, allowing for precise and automated control of the melt-release rate. During the metal melting process, the graphite rod is lowered via a control cabinet so

Table 1 Experimental researches for fuel-coolant interaction

Region (Institution)	Experimental facility or project	Triggering conditions	Objective
France (Scalian, Lab & CEA) & Japan (JAEA)	MELT facility	Self-trigger	Interactions between metallic corium jets and sodium
India (Homi Bhabha National Institute)	MFCI facility	Self-trigger	Fragmentation of simulated corium in sodium
Sweden (Royal Institute of Technology)	DEFOR-M facility	Self-trigger	Characteristics of a debris bed resulting from FCI
China (Sun Yat-Sen University)	PMCI facility	Self-trigger	Coolant Injection-mode
China (Xi'an Jiao Tong University)	Debris bed formation experimental platform	Self-trigger	The formation of the debris bed
This work China (Shanghai University of Electric Power)	External trigger experimental platform	Self-trigger & external trigger	Characteristics of triggering stage and triggering mechanism

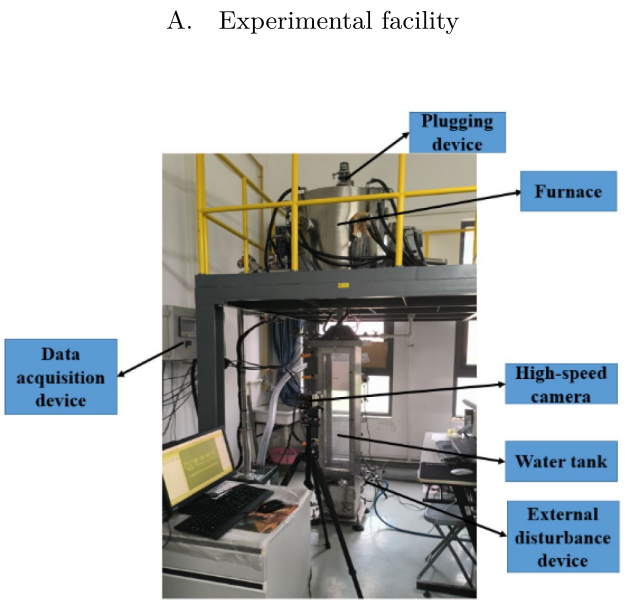

Fig. 1 (Color online) The overall experimental apparatus

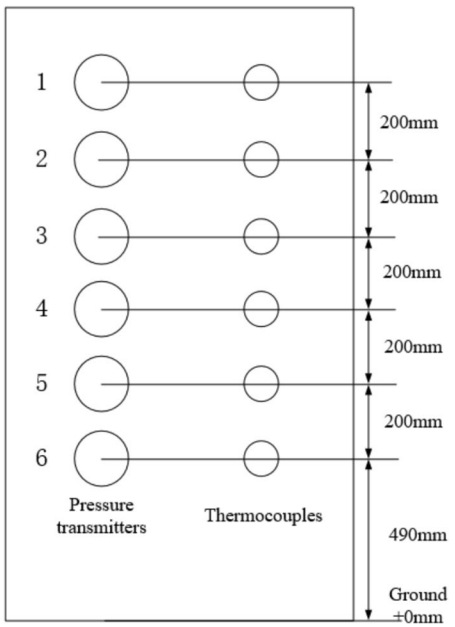

Fig. 2 Location of temperature and pressure measuring points

that its conical tip tightly seals against the corresponding conical outlet at the bottom of the graphite crucible, preventing leakage. Once the metal reaches the target temperature, the graphite rod is retracted upward by the control system, enabling the melt to be released and fall freely under the effect of gravity.

The water tank is a rectangular stainless-steel frame fitted with transparent viewing panels. To facilitate observation and data recording, the front and rear sides are equipped with pressure-resistant acrylic windows. The left-side wall features two rows of ports for mounting pressure transmitters and thermocouples. Figure 2 shows the vertical arrangement of the temperature and pressure measurement points. The internal dimensions of the tank are 250 mm (length) × 250 mm (width) × 1800 mm (height). The specifications of the measurement equipment used in this study are listed in Table 2. The bottom of the tank is equipped with a fragment collector and an electric heating unit, which are used for retrieving debris to analyze particle size distribution and heating the coolant water, respectively.

The temperature and pressure acquisition system comprises thermocouples, pressure transmitters, and a corresponding data acquisition platform, enabling the comprehensive recording of temperature and pressure variations during the melt settling in water. Additionally, a high-speed camera capable of frame rates of up to 200,000 fps, along with its supporting software, meets the requirements for the dynamic recording and image processing of the melt descent process.

The external disturbance device is shown in Fig. 3, comprises a gas cylinder (1), a pressure reducing valve (2), a trigger switch (3), a pressure relief switch (4), piston components (5), pressure transmitters (6), and other associated parts. Its operating principle involves regulating high-pressure gas from the cylinder via a pressure reducing valve. The regulated gas was then delivered through the trigger switch to the piston assembly located at the bottom of the water tank, generating a controlled external pressure pulse. This system enables the precise generation of millisecond-scale pressure disturbances of up to 3 MPa within a water environment, offering a safer and more stable alternative to traditional methods of introducing explosive disturbances [43, 44].

2.2 Case details and data processing

This study focused on the influence of external disturbances on the evolution characteristics of droplets during the triggering stage. A comparative experimental analysis of the transient velocity and expansion rate of droplets with and without external disturbance provides supporting evidence for understanding the droplet triggering mechanism. The materials and experimental conditions used are listed in Tables 3 and 4, respectively. The experimental procedure was as follows: Prior to each test, a predetermined amount of cooling water was added to the tank to maintain a consistent droplet falling height across all cases. The initial droplet temperature, water temperature, and external disturbance pressure were then set according to the requirements of each test condition. Once the target temperatures were reached, the melt-release device was activated to discharge the droplet. Data recording was simultaneously initiated using the

Table 2 Detailed information of the measuring equipment

Measuring equipment	Type	Range	Accuracy	Response time
Thermocouple	K-type	0–100 °C	±1%	1 s
Pressure transmitter	YMC-41	0–1 MPa	±0.1%	5 μs
High-speed camera	M230	200000 fps (at most)	1920×1080 (full resolution)	0.1 ms

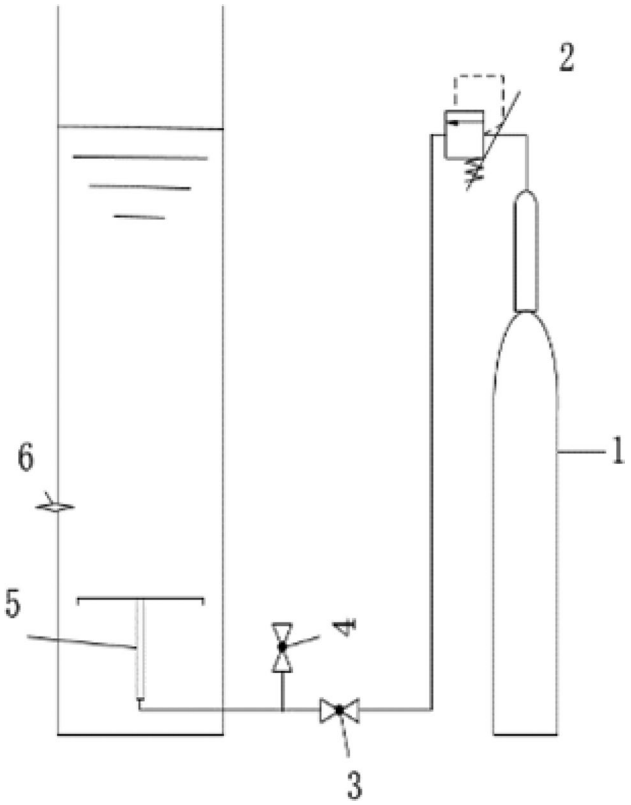

Fig. 3 Schematic diagram of external disturbance device. Gas cylinder (1), pressure reducing valve (2), trigger switch (3), pressure relief switch (4), piston components (5), pressure transmitters (6)

temperature and pressure acquisition system and a high-speed camera.

Controlling uncertainties in FCI experiments remains challenging because of the complex coupled hydrodynamic and thermal effects occurring within extremely short timeframes. Therefore, strict pre-test protocols are essential. During the pre-test preparation, an infrared pyrometer was used to accurately monitor the melt temperature in the furnace. The molten droplet was released only after the temperature remained stable for at least 15 min, limiting the maximum relative error in the droplet temperature to within 5%. To minimize impurities, all tests employed high-purity materials: Sn–99.99%, Pb–99.999%, and a Pb-Sn alloy with a composition of 50:50 wt%. These high-purity materials ensure consistent thermal properties of the melt. Although the droplet size (particularly droplet shape) cannot be precisely controlled and may influence local heat transfer and related processes, certain measures were taken to improve repeatability. As with other internationally recognized FCI experiments (e.g., MISTEE by KTH, KROTOS by CEA, TROI by KAERI, and SIGMA by UCSB), perfect reproducibility is not always achievable. Nevertheless, to promote droplet uniformity, an adjustment rod was used to regulate both the release frequency and droplet diameter. During preliminary tests, the rod was rotated until a stable stream of freely falling droplets was achieved—set here at 100 drops per minute. The rod position corresponding to this stable condition was marked and used in all subsequent tests to ensure essentially consistent droplet size.

Figure 4(a) shows two consecutive frames captured during droplet entry into water, with a time interval of 0.1 ms between frames.

The settling velocity was determined from close-range experimental observations. The transient velocity of the droplet was estimated by calculating the average velocity between two consecutive images, which is defined as the ratio of the relative displacement to the time interval. The leading-edge position of each droplet was tracked using a high-speed video, and the displacement (denoted as $\triangle y$) over a 0.1 ms interval (corresponding to the system response time) was recorded. Therefore, the corresponding velocity is given by Eq. (1).

Table 3 Main properties of the experimental materials

Experimental materials	Density (g/cm^3)	Melting point (°C)	Boiling point (°C)	Specific heat capacity (J/(kg·K))
Tin	7.28	232	2260	228
Lead	11.34	328	1740	130
Lead-tin alloy	8.90	183	1620	180

Table 4 Experimental conditions

Test	Experimental materials	Temperature of melt (°C)	Temperature of water (°C)	External disturbance pressure (MPa)
A1	Lead-tin alloy	300	20	–
A2	Lead-tin alloy	400	20	–
A3	Lead-tin alloy	500	20	–
A4	Lead-tin alloy	600	20	–
A5	Lead-tin alloy	700	20	–
A6	Lead-tin alloy	800	20	–
B1	Lead-tin alloy	500	50	–
B2	Lead-tin alloy	500	80	–
C1	Tin	500	20	–
C2	Lead	500	20	–
D1	Lead-tin alloy	500	20	1
D2	Lead-tin alloy	500	20	2
D3	Lead-tin alloy	500	20	3
D4	Lead-tin alloy	500	50	3
D5	Lead-tin alloy	500	80	3
D6	Lead-tin alloy	300	20	3
D7	Lead-tin alloy	800	20	3
D8	Tin	500	20	1
D9	Tin	500	20	2
D10	Tin	500	20	3
D11	Lead	500	20	1
D12	Lead	500	20	2
D13	Lead	500	20	3

$$v = \frac{\triangle y}{0.1 \times 10^{-3}} \tag{1}$$

Figure 4(b) shows the droplet shape at a specific instant during water entry. Although the shape change of the droplet within the mixing region could not be precisely quantified from the image, the boundary of the interaction zone was clearly distinguishable. Therefore, the instantaneous droplet diameter was approximated based on an equivalent circular area, and the droplet expansion rate was taken as the average expansion rate between two consecutive images. The equivalent diameter of the molten droplet was estimated using the following Eq. (2), where D_x and D_y represent the horizontal and vertical diameters of the droplet, respectively, and D_d denotes the equivalent diameter [1] used to characterize the size of the irregularly shaped droplet.

$$D_\mathrm{d} = (D_x^2 D_y)^{\frac{1}{3}} \tag{2}$$

The droplet expansion rate was determined by analyzing high-speed video footage of the vapor film-water interface evolution. Using the equivalent diameter method, the instantaneous droplet diameter was measured over a 0.1 ms interval (system response time). Therefore, the corresponding expansion rate is given by Eq.(3).

$$v_\mathrm{er} = \frac{D_\mathrm{d}^{t+1} - D_\mathrm{d}^{t}}{0.1 \times 10^{-3}} \tag{3}$$

Experimental measurements are inevitably subject to discrepancies from true values owing to factors such as instrument accuracy, measurement techniques, and test conditions. In this study, measurement errors were categorized as direct or indirect. For parameters with direct measurement errors, the true value is expressed as Eq. (4):

$$X_\mathrm{real} = X \pm \varphi, \tag{4}$$

where X_real is the true value of the parameter, X is the measured value of the parameter, φ is the absolute error of this parameter.

The physical variables directly measured are $X_1, X_2, X_3, \ldots, X_n$, because $X_1, X_2, X_3, \cdots, X_n$ are independent variables. The indirect measurement of the physical variable is G, which is given by the following relationship:

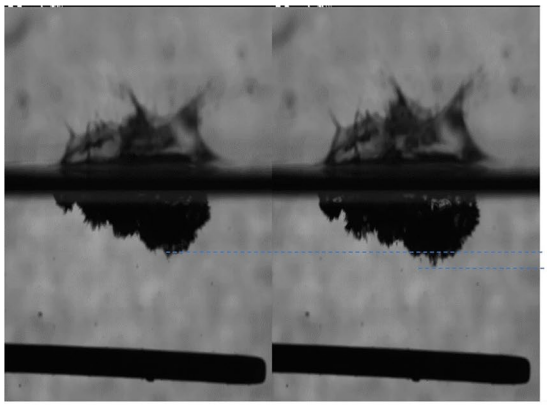

(a)

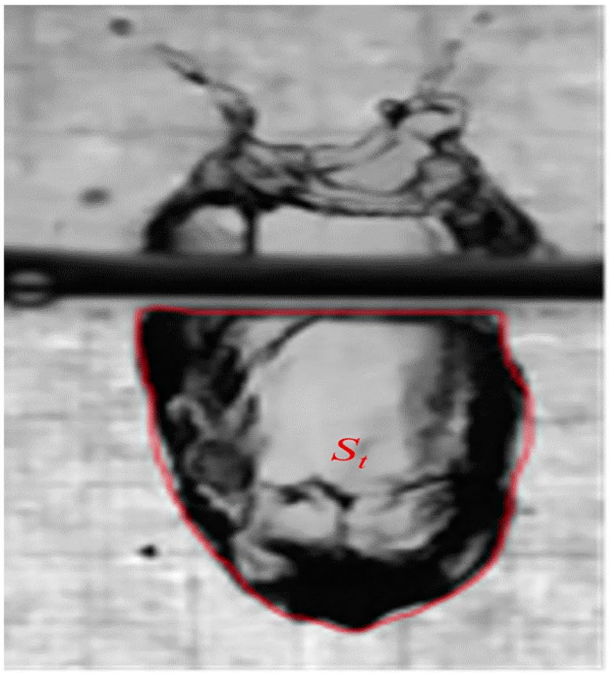

(b)

Fig. 4 Processing of the images. **a** Instantaneous droplet motion; **b** instantaneous interaction between a droplet and water

$$G = S(X_1, X_2, X_3, \ldots, X_n). \tag{5}$$

For parameters with indirect measurement errors, based on the error transfer theory, the error of the physical variable by indirect measurement can be calculated using the following Eq. (6):

$$\varphi_G = \sqrt{\left(\frac{\delta S}{\delta X_1}\right)^2 \varphi_{X_1}^2 + \cdots + \left(\frac{\delta S}{\delta X_n}\right)^2 \varphi_{X_n}^2}, \tag{6}$$

Table 5 Relative errors

Parameters	Maximal relative error
Droplet mass	2.0%
Droplet temperature	5.0%
Water temperature	1.0%
Pressure change during interaction	2.0%
Temperature change during interaction	1.0%
External disturbance pressure	2.0%
Transient droplet velocity	3.5%
Droplet expansion rate	1.3%

where φ_G is the error of the indirectly measured physical variable, φ_{X_i} is the error of the direct measurement value X_i, $\frac{\delta S}{\delta X_i}$ is the error transfer coefficient.

Therefore, the relative error of the indirectly measured physical variable G during the experiment is given by Eq.(4):

$$\psi = \frac{\varphi_G}{G}. \tag{7}$$

Based on the error calculation methodology described above, the maximum relative errors for the key experimental parameters, including the droplet mass, droplet temperature, water temperature, pressure variations during the interaction, external disturbance pressure, droplet settling velocity, and droplet expansion rate, are presented in Table 5.

3 Results and discussion

3.1 Typical phenomena

The A1 condition, characterized by a lead-tin alloy temperature of 300 °C, water temperature of 20 °C, and absence of external disturbance pressure, is illustrated in Fig. 5(a). The penetration event was of short duration. Prior to water contact, the droplet fell in a regular shape. The immense temperature difference upon impact induces violent heat transfer, resulting in the formation of a vapor film that encapsulates the droplet. Subsequent expansion of the vapor was observed in both the horizontal and vertical directions, yielding a vapor pocket. A pronounced separation of this pocket from the droplet occured in the vertical direction, in contrast to the more limited horizontal development. Air entrainment, which is attributed to the droplet-water velocity difference, was also observed. As presented in Fig. 5(b), the vapor pocket subsequently undergoes constriction at its center, with the majority of the entrained air migrating

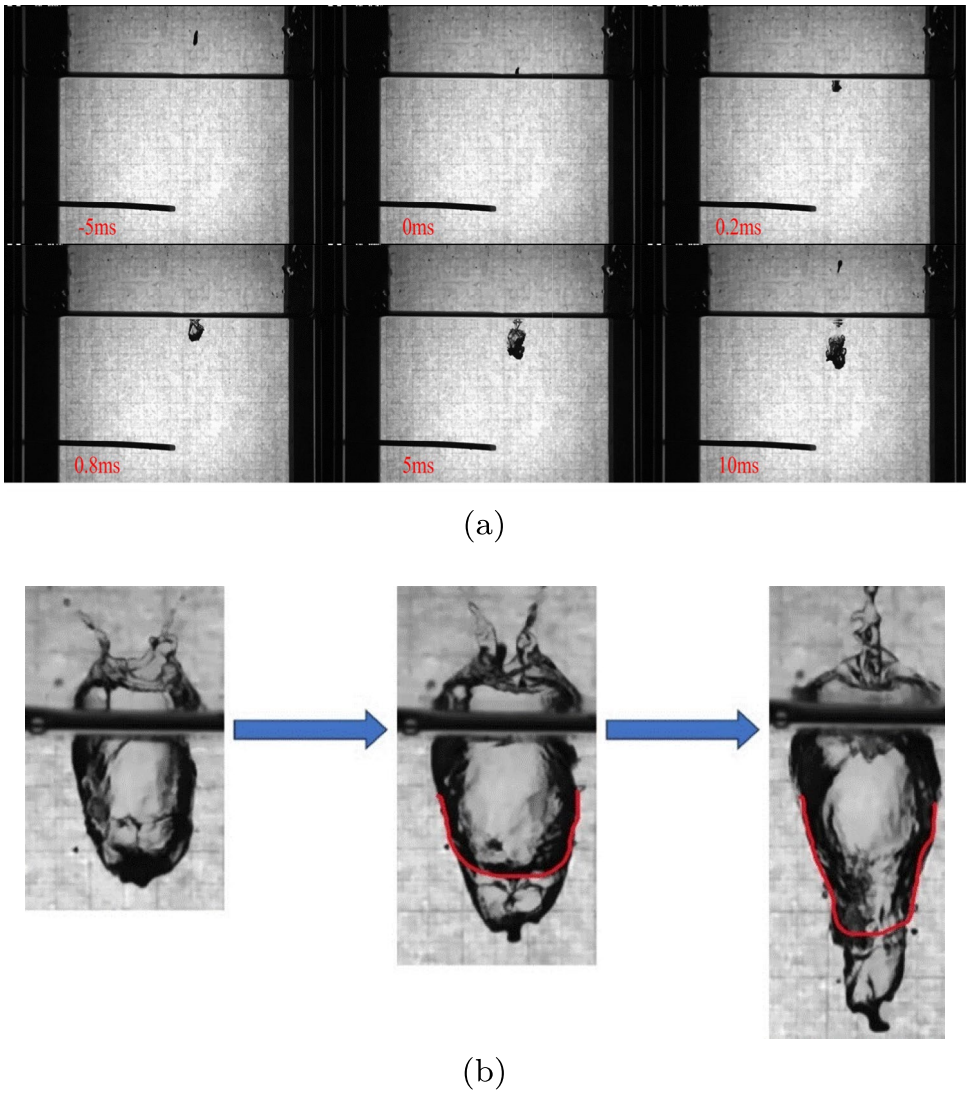

Fig. 5 Image processing. **a** Diagram of droplet motion; **b** Air entrainment phenomenon

backwards under aqueous surface tension until atmospheric release.

Figure 6(a) shows the transient velocity variation of a droplet. In the plot, line a-b corresponds to the droplet velocity change in air. The water surface is indicated by a solid black line, and the moment at which the droplet crosses this line is defined as $t = 0$ s for simplicity. Line b-c reflects the velocity variation during the initial penetration into the water. Upon contacting the water, the droplet experiences deceleration owing to both hydrodynamic drag and an upward force caused by localized steam generation at the leading edge, resulting in an increase in pressure. As steam generation increases over time, the pressure at the front of the droplet increases, forcing the vapor to move rearward and form an airbag along with the entrained air. As demonstrated in our previous study [45], this vapor envelope reduces drag, resulting in a velocity recovery, as shown by line c-d. When the vapor shifted backward, the droplet's leading edge reestablished contact with the liquid water. Although some steam continues to form, its quantity is reduced, and the stability is diminished. Consequently, the hydrodynamic resistance increased again, and the droplet velocity decreased, as shown in line d-e. Finally, as the droplet detaches from the airbag and undergoes further deformation, its velocity continues to decline until it stabilizes, as represented by the line e-f.

Figure 6(b) shows the expansion rate history of the same droplet. Line a-b corresponds to the period from the initial water contact to full submersion. The vapor generated by intensive droplet-water heat transfer causes droplet expansion. However, because the immersion process initially occurs at a low velocity and the wetted area of the droplet increases only gradually, a stable interaction state is not yet reached. Thus, the expansion rate increased only slowly during this stage. Line b-c corresponds to a faster immersion phase, during which the airbag at the droplet leading edge

Fig. 6 Data processing

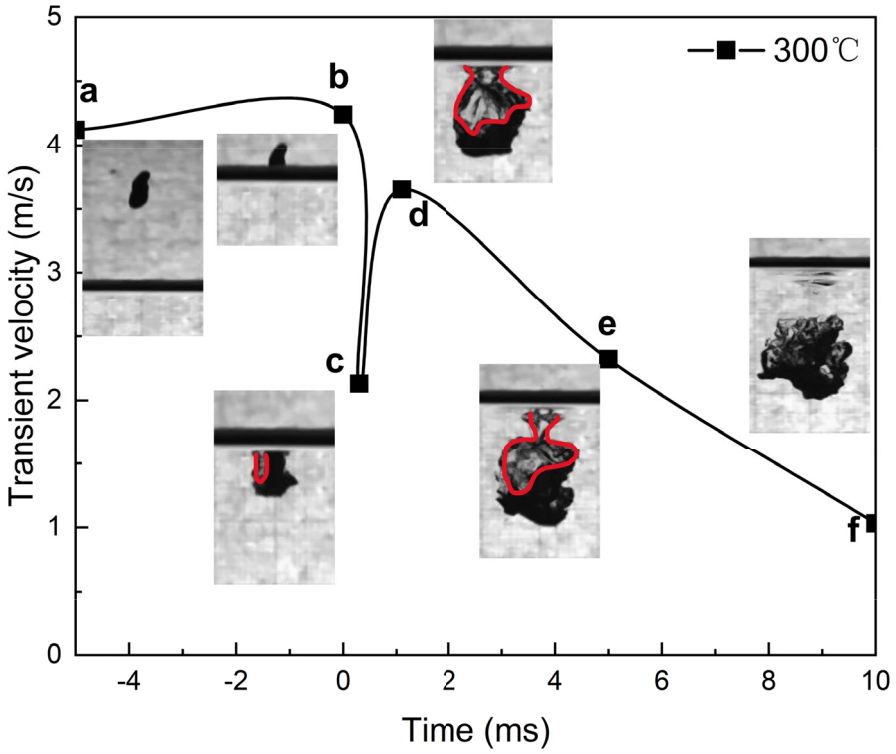

(a) Transient velocity

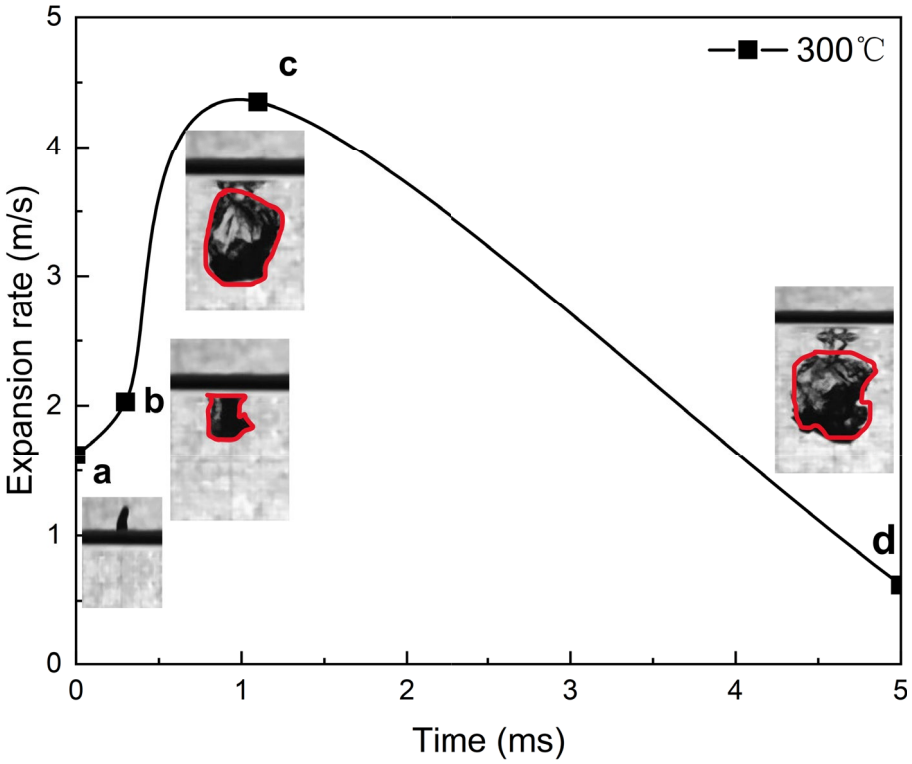

(b) Expansion rate

began to collapse. The droplet may also undergo expansion and fragmentation upon contact with cold water, leading to a sharp rise in the expansion rate. However, over time, the droplet cooled and the airbag detached, causing the expansion rate in line c-d to gradually decline toward zero.

3.2 No external disturbance pressure

Figure 7(a) shows the transient velocity of a single droplet at different temperatures upon contact with water. As the droplet temperature increased, the duration of acceleration and peak velocity were extended and elevated, respectively, thereby raising the overall velocity level. At a constant water temperature, a hotter droplet induces faster and more extensive water evaporation, producing more vapor. This influences the process in two ways. First, enhanced evaporation accelerates cavity formation, prolonging the droplet's fall within the cavity. As previously analyzed, the cavity reduces the direct contact between the droplet and water, leading to lower resistance and thus a higher droplet velocity. Second, more vapor accumulates in the droplet's wake region [46], providing additional downward propulsion. Figure 7(b) presents the droplet expansion rate across different droplet temperatures. As the temperature rises, the growth duration of the expansion rate after water entry was prolonged, whereas the peak expansion rate initially increased and then decreased. At 300 °C, the droplet was rapidly cooled upon contact, resulting in only a minor increase in the expansion rate. At 400 °C, 500 °C, and 600 °C, the droplet enters an unstable film boiling regime, where intermittent vapor film collapse causes repeated water contact and fine-scale fragmentation, leading to large fluctuations in the expansion rate. At 700 °C and 800 °C, stable film boiling occured, enveloping the droplet in a persistent vapor film that protected it during descent until cooling. Here, the expansion rate increased smoothly and exhibited the longest duration among all cases. Figure 7(c) illustrates transient thermal-hydraulic behavior and resulting debris fragments at droplet temperatures of 300 °C, 500 °C, and 700 °C. At 300 °C, the droplet's leading edge develops a conical protrusion, and the resulting debris fragment is smooth and elliptical. At 500 °C, the leading edge becomes flared and spiky, and the debris body appears rough and curled. At 700 °C, the leading edge reverts to a smooth elliptical shape, while the debris fragments form slender, flake-like structures with spiky surfaces. In addition, the peak pressures measured by a high-frequency dynamic pressure transducer further supported these observations, showing a trend of initial increase followed by a decrease with rising droplet temperature. The maximum pressure, 0.022 MPa, occurs at 500 °C, as summarized in Table 6. Additionally, by comparing the timing of the transient velocity and expansion rate, it is noteworthy that their peak values occur simultaneously.

Figure 8(a) shows the transient velocity of a single droplet at different coolant temperatures. As the coolant temperature increased, the acceleration period of the droplet lengthened,

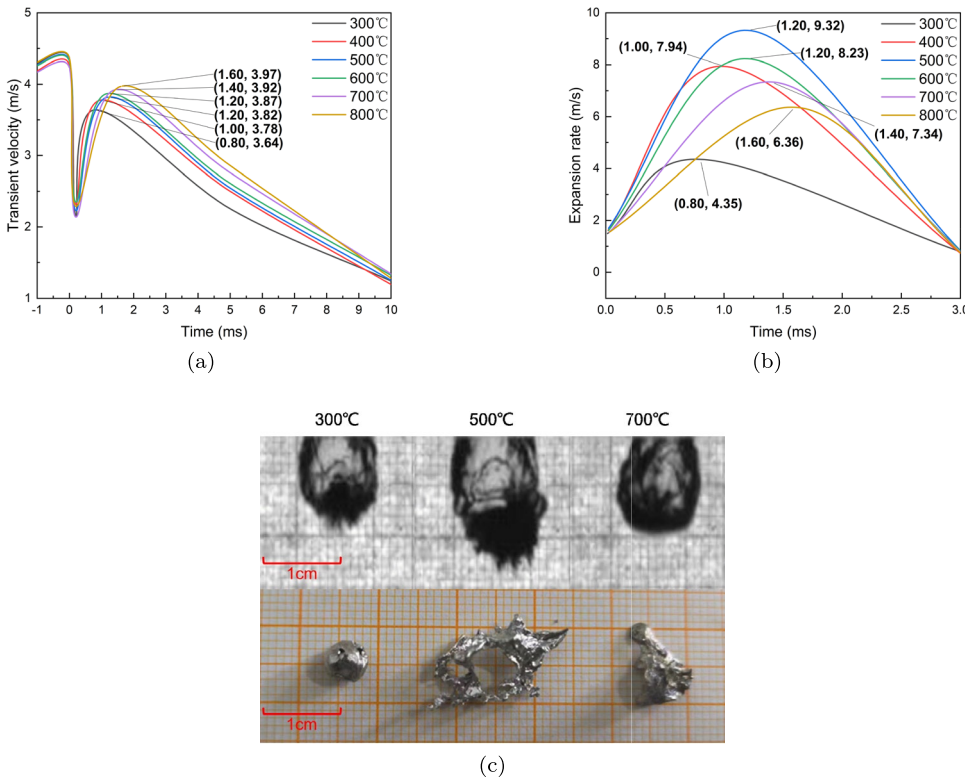

Fig. 7 (Color online) Different droplet temperatures. **a** Transient velocity; **b** expansion rate; **c** experimental phenomena and products

Table 6 The peak pressure at different droplet temperatures

Test	Time (ms)	Peak pressure (MPa)
A1	0.82	0.002
A2	1.04	0.018
A3	1.24	0.022
A4	1.27	0.016
A5	1.49	0.011
A6	1.64	0.008

and its peak velocity also rised. This behavior is analogous to the effect of the droplet temperature described earlier. When the droplet temperature was fixed, a higher coolant temperature allowed the water to reach boiling more readily, leading to a prolonged evaporation time, higher evaporation rate, and greater total vapor volume. This promoted the formation of a protective cavity that propelled the droplet downward. Figure 8(b) presents the droplet expansion rate under different coolant temperatures. Although the duration of the expansion rate growth lengthens with increasing coolant temperature, the peak expansion rate decreases. At 20 °C, the droplet experiences unstable film boiling, where the vapor film collapses intermittently, causing repeated contact with water and fine fragmentation. As the water temperature rises, the heat transfer shifts toward stable film boiling, forming a persistent cavity that shields the droplet during its descent until cooling. Consequently, the expansion rate increased gradually, and the growth period became the longest of all treatments. Figure 8(c) shows representative phenomena and resulting debris at coolant temperatures of 20 °C, 50 °C, and 80 °C. With increasing coolant temperature, the droplet's leading edge became more rounded, and the resulting debris fragments became smoother. This occurs because more vapor is generated over the same period as the coolant temperature rises, creating a more stable cavity that envelops the droplet, reduces direct water contact, and limits deformation. Peak pressure measurements obtained using a dynamic high-frequency pressure transducer further supported these observations. As listed in Table 7, the peak pressure decreased with increasing coolant temperature. Finally, consistent with earlier findings, the moment of the peak transient velocity coincided with that of the expansion rate.

Table 7 The peak pressure at different water temperatures

Test	Time (ms)	Peak pressure (MPa)
A3	1.24	0.022
B1	1.46	0.013
B2	1.69	0.006

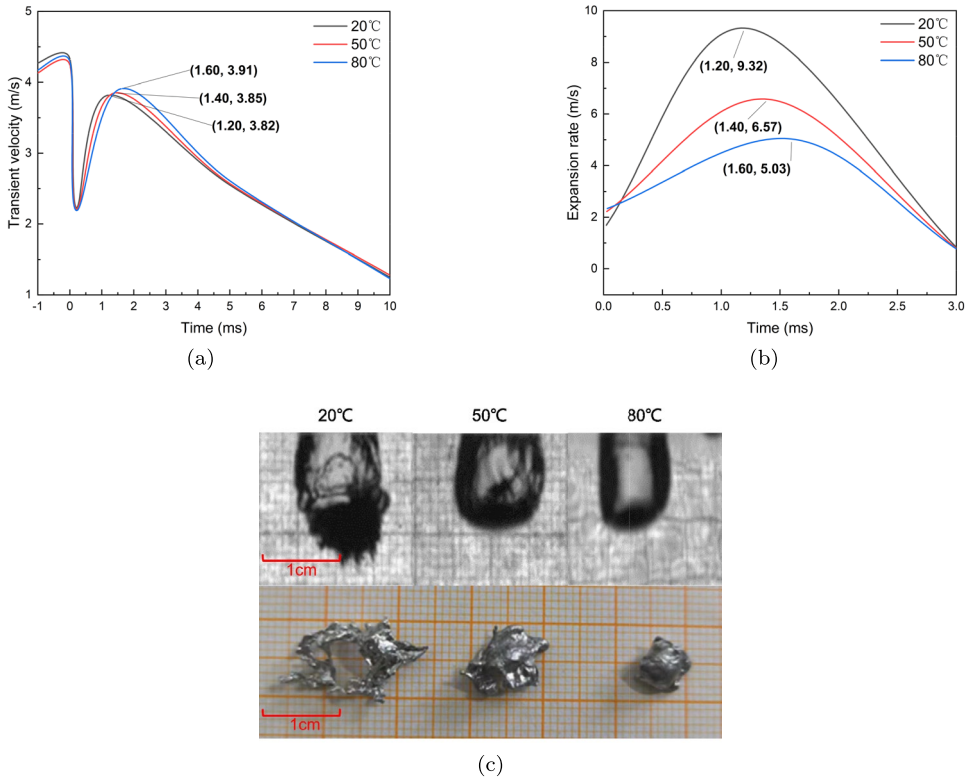

Fig. 8 (Color online) Different water temperatures. **a** Transient velocity; **b** Expansion rate; **c** Iconic phenomena and product fragments

Figure 9(a) shows the transient velocity of the droplets for different materials. The lead-tin alloy droplet reached the highest peak velocity upon entering the water. This occurs because of the lower melting point of the alloy, which allows it to store more internal energy at the same temperature. Consequently, water evaporated more readily, and a larger volume of vapor was generated, increasing the peak transient velocity of the droplet. Figure 9(b) presents the expansion rate for each material. The lead-tin alloy and tin droplets exhibited significant fluctuations in the expansion rate, whereas the lead droplet remained largely stable. This further suggests that under identical conditions, lead is less susceptible to vapor explosions. Figure 9(c) shows the typical experimental phenomena and resulting debris for the lead-tin alloy, tin, and lead. Owing to its higher melting point, lead has a lower degree of superheating at the same temperature, making it less prone to fine fragmentation. Peak pressure measurements support this observation, with values decreasing in the order of lead-tin alloy > tin > lead, as summarized in Table 8. Consistent with earlier results, the moment of the peak transient velocity coincided with that of the peak expansion rate.

3.3 External disturbance pressure

The preceding analysis examined the laws governing the transient velocity and expansion rate of the droplets under self-triggering conditions. However, in severe accidents, various disturbances in the external environment can affect the triggering process of droplets. This section introduces external disturbances by setting a disturbance plate in motion at the bottom of the water tank, focusing on the impact of external disturbance pressure on the process, with specific conditions listed in Table 4. Figure 10 illustrates the motion of one single droplet under Test D6, where the lead-tin alloy is initialized at 300 °C, and the coolant is maintained at 20 °C, with the external disturbance pressure of 3 MPa. Before the lead-tin alloy droplet contacts the water surface, the water has already been initialized from the external disturbance pressure, as reflected by the bubbles moving upwards in Fig. 10. Compared with Test A1, after the lead-tin alloy droplet entered the water surface, its penetration depth at the same moment was significantly reduced owing to the action of the external disturbance, and the gas-liquid interface changes became more chaotic upon detachment from the water surface.

Figure 11 shows the transient velocity of the droplet under different external disturbance pressures. With the increase of the external disturbance pressure, the duration of the velocity increase of the droplet after penetrating the water decreased, and the peak velocity of the droplet also decreased accordingly. This is because after the droplet penetrated the water pool, the drag force can rapidly boost

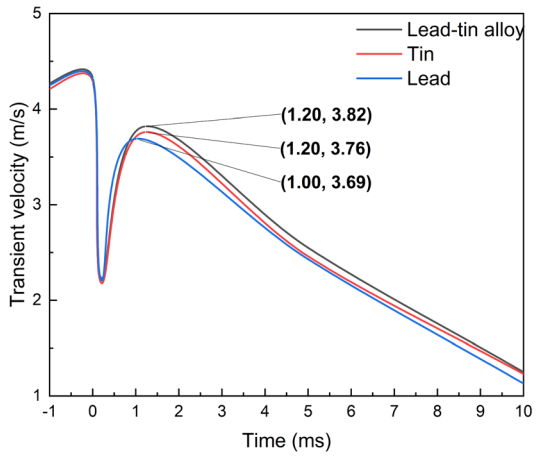

(a)

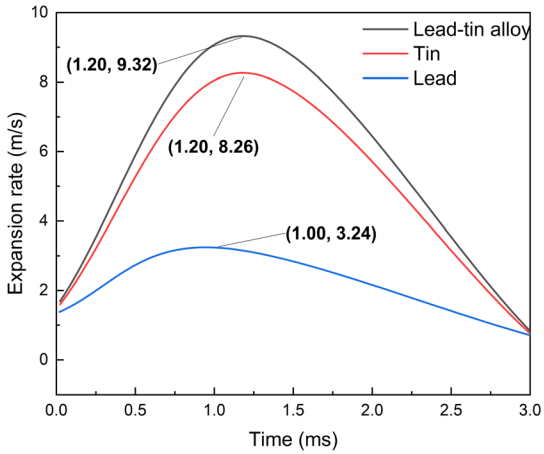

(b)

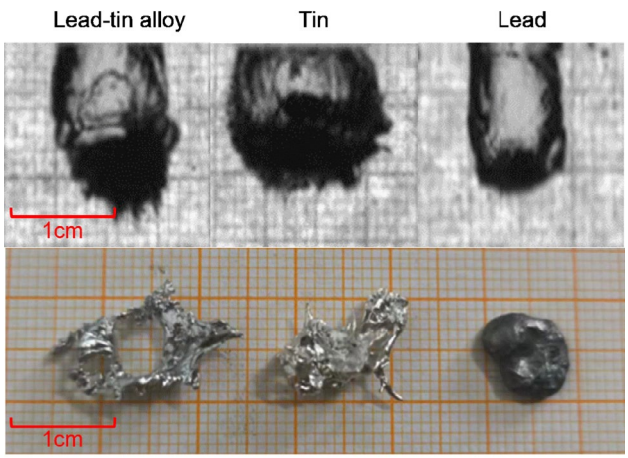

(c)

Fig. 9 (Color online) Different droplet materials. **a** Transient velocity; **b** Expansion rate; **c** Experimental phenomena and product debris

Table 8 The peak pressure at different droplet materials

Test	Time (ms)	Peak pressure (MPa)
A3	1.24	0.022
C1	1.27	0.019
C2	1.05	0.003

the decrease in velocity. Meanwhile, with the enhancement of heat transfer at the interface, the hot droplet turns to be surrounded by a thick layer of steam and air mixture, thus promoting the drag reduction in the subsequent droplets. This competition leads to an increase in the velocity of the hot droplet until the peak velocity is reached. Moreover, when an external disturbance pressure is introduced, it may weaken the stability of the gas layer, thus increasing the drag force. Therefore, as the external disturbance pressure increased, the peak pressure owing to the drag reduction decreased. Figure 12 shows the transient velocity comparison of lead-tin alloy droplet with or without external disturbance pressure at different droplet temperatures and water temperatures. The results also show that the external disturbance pressure can reduce the peak velocity of the droplets.

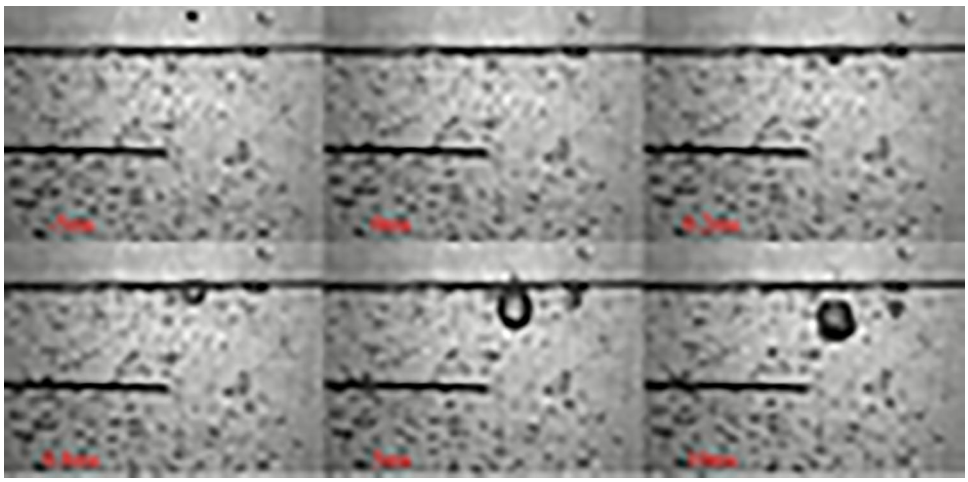

Fig. 10 Droplet motion process under external disturbance pressure

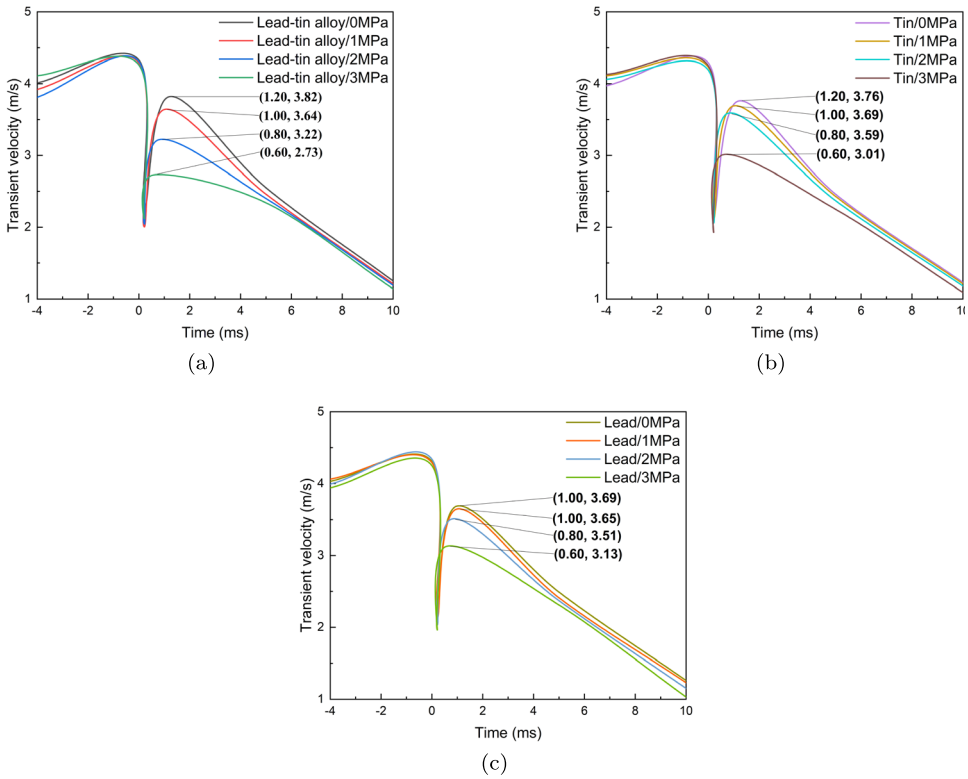

Fig. 11 (Color online) Droplet transient velocity under different external disturbance pressures. **a** Lead-tin alloy; **b** tin; **c** lead

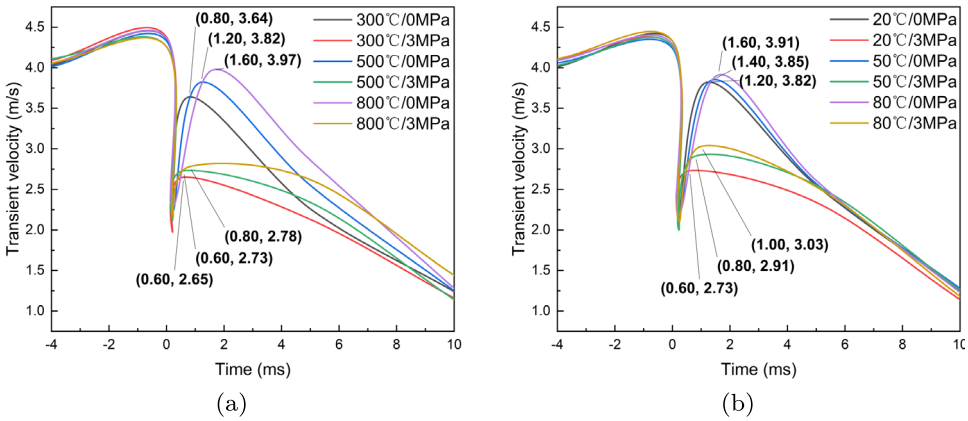

Fig. 12 (Color online) Comparison of transient droplet velocity of lead-tin alloy with or without external disturbance pressure. **a** Different droplet temperatures; **b** different water temperature

Moreover, under the external disturbance conditions, the initial temperature of the droplets may have less effect on the drag reduction of the droplets, and the external pressure dominates the settling process.

Figure 13 shows the droplet expansion rate under different external disturbance pressures. As the external disturbance pressure increased, the duration of the expansion rate after the droplet entered the water decreased; however, the peak expansion rate increased. Even for the case of the lead droplet, the expansion rate can reach up to 9.46 m/s, as shown in Fig. 13(c). This phenomenon occurs because as the droplet descends through the water, the initiation of the trigger at the interface leads to the fine-fragmentation process in some local regions. The resulting fine particles dispersed around the parent droplet, forming a gaseous film that contributed to the expansion of the hot droplets. When the external disturbance pressure propagates, it readily induces an increase in the instability of the droplet surface, thereby triggering further fine fragmentation. Compared to the self-trigger scenario, this localized fine-fragmentation process was more pronounced. Consequently, as the external disturbance pressure increased, the droplet expansion rate correspondingly escalated. Moreover, the cavity is more likely to collapse under the action of external disturbance pressure, which accelerates the contact time between the droplet and water, thereby increasing the degree of fine fragmentation

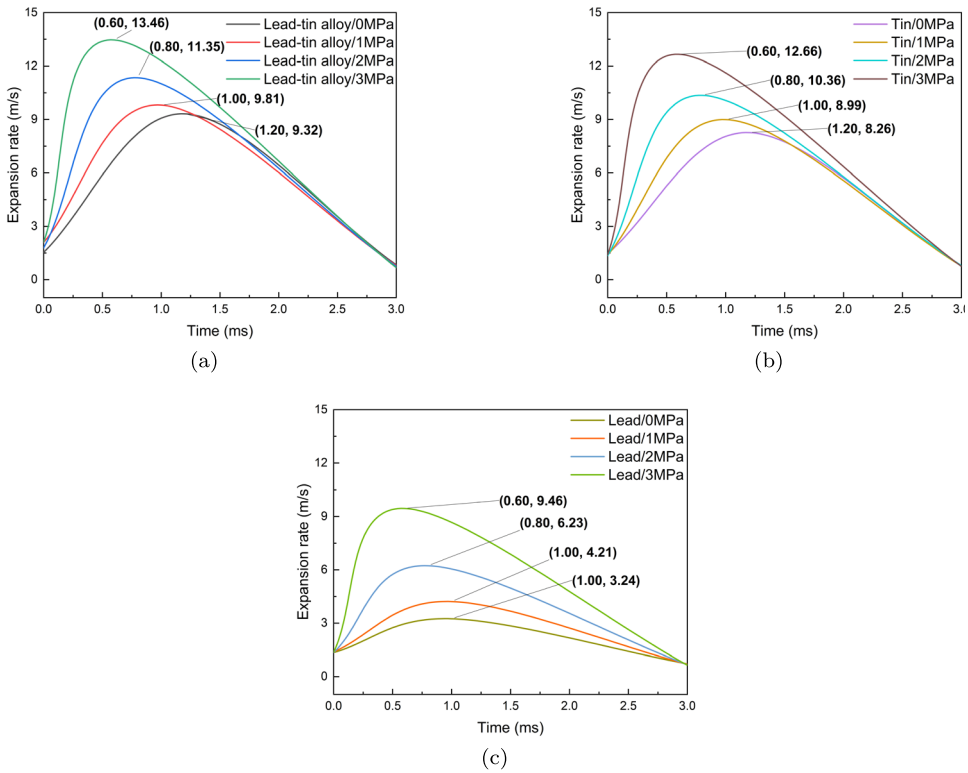

Fig. 13 (Color online) The droplet expansion rate under different external disturbance pressures. **a** Lead-tin alloy; **b** Tin; **c** Lead

of the droplet, as shown in Fig. 14. Figure 15 shows a comparison of the expansion rate of lead-tin alloy droplets with and without external disturbance pressure at different droplet temperatures and water temperatures. The results also show that the external disturbance pressure can reduce the rise time of the droplet expansion rate and increase the peak value of the expansion rate. In addition, with an increase in the initial temperature of the droplet or the coolant temperature, the external disturbance pressure can further promote the triggering process. The highest growth rate can be achieved by 108% when the coolant temperature is approximately 80 °C. Therefore, attention should be paid, although it is very close to the saturation condition for real severe accidents, when an external trigger may occur. Figure 16 shows the mass ratio of product fragments with diameters of less than 0.5 mm under different working conditions. With an increase in the external disturbance pressure, the mass ratio of product fragments with diameters less than 0.5 mm also increased. Simultaneously, the peak pressure measured by the dynamic high-frequency pressure transmitter in the

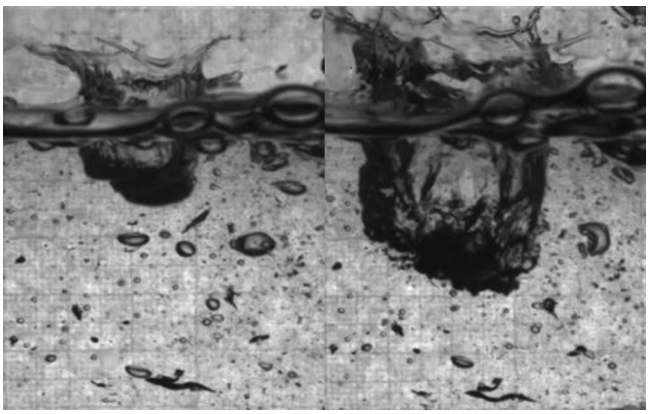

Fig. 14 The steam film at the leading edge of the droplet is collapsing under the action of external disturbance pressure

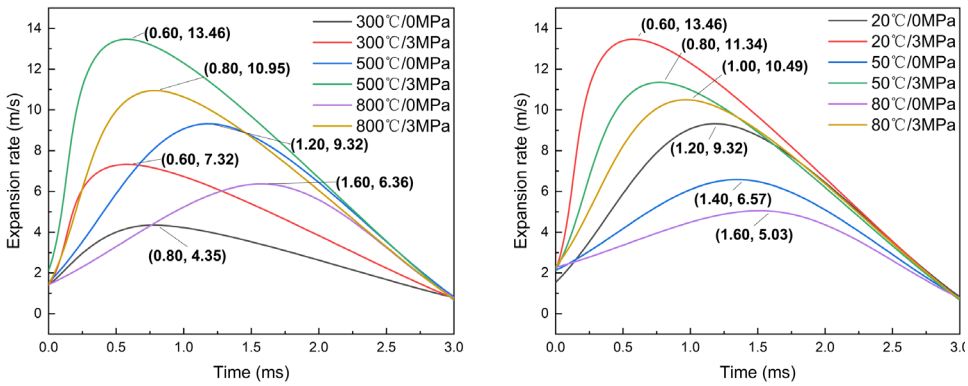

Fig. 15 (Color online) Comparison of droplet expansion rate of lead-tin alloy with and without external disturbance pressure. **a** Different droplet temperatures; **b** Different water temperature

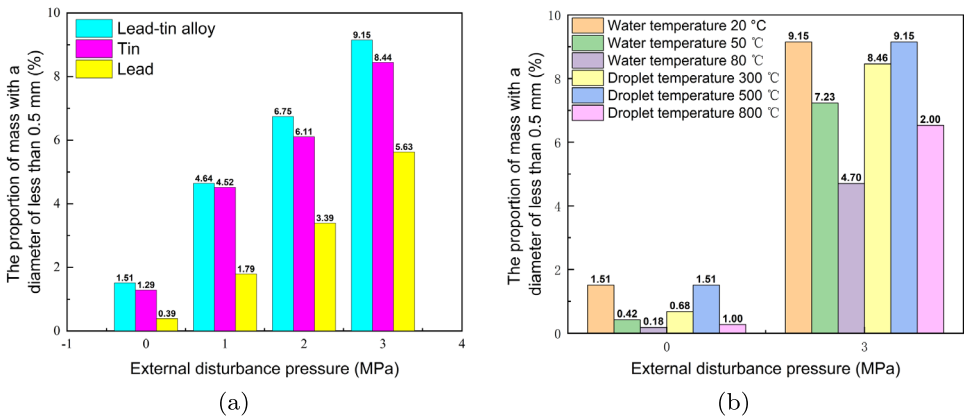

Fig. 16 (Color online) The mass ratio of product fragments with a diameter of less than 0.5 mm under different working conditions. **a** Type of material; **b** Water and droplet temperature

experiment also illustrated this phenomenon, as shown in Table 8. As the external disturbance pressure increased, the peak pressure values exhibited an ascending trend. Conversely, as the coolant temperature increased, the peak pressure values exhibited a descending trend. Furthermore, an increase in the droplet temperature was associated with a biphasic trend in the peak pressure values, which initially increased and subsequently decreased. Ultimately, a comparative analysis of the transient velocity and expansion rate moments revealed that the peak transient velocity moment was synchronized with the peak expansion rate moment.

Another important point to address is that the primary factor influencing the measured pressure variation is the distance between the measurement point and molten droplet. As pressure propagates from the local triggering region, it is attenuated by water resistance. The pressure decay can be estimated using the following Eq. (8), where P and P_0 refer to the triggering pressure at the measuring point and the surface of the molten droplet, respectively, r refers to the distance between the measuring point and the location of the molten droplet at the triggering time, b refers to the empirical coefficient, which is usually regarded as 1.03 in water. Using this equation, the corresponding peak pressure at the droplet surface can be effectively reconstructed. For instance, in Test A3 and Test D3, the measured triggering pressures were 0.022 MPa and 0.081 MPa, respectively. After applying the correction, the estimated pressures at the droplet surface were approximately 0.57 MPa and 2.1 MPa. These results demonstrate that the applied external disturbance significantly enhanced the trigger pressure compared to the spontaneous triggering conditions.

$$P = P_0 r^{-b} \tag{8}$$

3.4 Comparison with previous work and limitations of the present work

A recent study by KTH in Sweden [47] examined steam explosion characteristics involving multiple molten tin droplets falling through a coolant pool. This configuration is highly similar to that in the present study, in which streams of molten Sn, Pb, and Sn-Pb alloy droplets descend through a coolant pool. The authors reported distinct and complex steam explosion behaviors not observed in earlier single-droplet experiments, an important finding given the limited available data on multi-droplet configurations and the clear need for deeper investigation into such conditions.

In their tests, a spontaneous steam explosion was initiated, and triggered explosions were speculated to occur subsequently; however, the underlying mechanism remains unclear. In the present study, external triggering was reliably achieved by applying an external disturbance pressure in direct contact with the molten droplets. Notably, even lead, a material known for its resistance to explosions, could be triggered under a 3 MPa external disturbance, generating a peak pressure of 64 kPa.

It should also be noted that, owing to the relatively similar mass of Sn droplets used in the experiments, the peak pressures ranged from 1 to 33 kPa (as shown in Fig. 9) were obtained for different initial melt masses. In the present study, Sn was used in cases C1, D8, D9, and D10. For the internally triggered case, a peak pressure of 19 kPa was recorded, whereas the externally triggered cases yielded peak pressures of 26 kPa, 49 kPa, and 47 kPa, as shown in Table 9, which align reasonably well with earlier experimental results from KTH (Fig. 17).

In summary, this study focused primarily on the triggering behavior of small-scale molten droplets at temperatures up to 800 °C, a range compatible with high-speed visualization. However, evidence [40] suggests that higher-melting-point materials may undergo significantly different fuel-coolant interactions, potentially altering the steam explosion strength. Moreover, the explosion behavior of these materials under external triggering remains complex and inadequately understood. Additionally, because of obscuration by the vapor envelope, the droplet-gas interface could not be clearly resolved with high-speed imaging. Consequently, the expansion rates could only be estimated approximately from the extent of the gas phase. X-ray imaging is a promising alternative for tracking internal structures during FCI, particularly for high-melting-point materials. As such materials

Table 9 The peak pressure under different working conditions

Test	Time (ms)	Pressure peak (MPa)
A3	1.24	0.022
D1	1.06	0.034
D2	0.81	0.052
D3	0.64	0.081
C1	1.27	0.019
D8	1.08	0.026
D9	0.83	0.049
D10	0.66	0.074
C2	1.05	0.003
D11	1.09	0.016
D12	0.86	0.034
D13	0.69	0.064
D3	0.64	0.081
D4	0.85	0.056
D5	1.03	0.034
D6	0.67	0.047
D3	0.64	0.081
D7	0.82	0.034

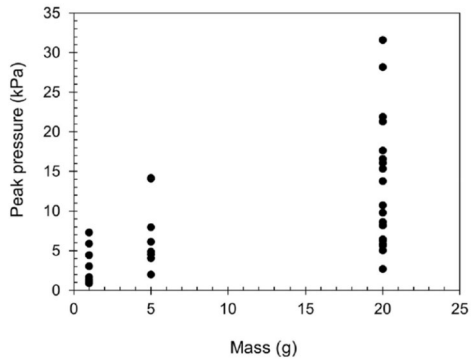

Fig. 17 Peak pressure of steam explosion against melt sample initial mass [47]

cool, rapid crust formation [12] may influence the interaction more strongly than external triggers. Understanding how these mechanisms compete and interact will be the key focus of our subsequent research.

4 Conclusion

This study investigated the behavior of molten droplets during fuel-coolant interactions under external disturbance conditions using a self-designed FCI experimental facility. The transient velocity, expansion rate, dynamic phenomena, debris characteristics, and peak pressures under various conditions were analyzed in detail. The main findings are as follows:

(1) The analysis of droplet transient velocity revealed that cavity formation reduced droplet resistance, leading to an increase in peak velocity. In the absence of external disturbances, higher droplet and coolant temperatures promoted faster and more stable cavity formation, resulting in a rising trend in the peak droplet velocity. However, under external disturbance, increased disturbance pressure makes the cavity more prone to collapse, and the peak droplet velocity decreases accordingly.

(2) The evaluation of the droplet expansion rate showed that without external disturbance, the peak expansion rate initially increased and then decreased with an increase in the droplet temperature, whereas it decreased with an increase in the coolant temperature. Under external disturbance, the peak expansion rate increased with the disturbance pressure. At 3 MPa external pressure, the peak expansion rate more than doubled.

(3) Based on the trigger pressure peaks and debris morphology, external disturbances appear to shorten the triggering time of the droplet surface and enhance the triggering intensity. This requires particular attention in severe accident scenarios close to saturation conditions, where external triggers may be present.

This study serves as the first part of a broader investigation into the effect of external disturbances on molten droplet triggering. Newly observed phenomena such as air entrainment and its influence, as well as the interplay between vapor-induced drag reduction and external disturbance, will be further examined through theoretical modeling. The current data on peak velocity, expansion rate, and peak pressure provide a valuable database for validating subsequent theoretical and numerical models. Incorporating these phenomena into simulation codes, such as MC3D or SIMMER, will improve the interpretation of FCI processes and help reduce predictive uncertainties.

Author Contributions All authors contributed to the study conception and design. Material preparation, data collection and analysis were performed by He-Lin Chen, Cheng Peng and Xian-Pin Meng. The first draft of the manuscript was written by He-Lin Chen and Cheng Peng, and all authors commented on previous versions of the manuscript. All authors read and approved the final manuscript.

Data Availability The data that support the findings of this study are openly available in Science Data Bank at https://cstr.cn/31253.11.sciencedb.j00186.00863 and https://doi.org/10.57760/3sciencedb.j00186.00863

Declarations

Conflict of interest The authors declare that they have no conflict of interest.

References

1. M. Zhong, Z. Li, M. Lin et al., Numercial analysis of pressure load in a PWR cavity in an ex-vessel steam explosion. Nucl. Sci. Tech. **25**, 030601 (2014). https://doi.org/10.13538/J.1001-8042/NST.25.030601
2. T.G. Theofanous, The study of steam explosions in nuclear systems. Nucl. Eng. Des. **155**, 1–26 (1995). https://doi.org/10.1016/0029-5493(94)00864-U
3. L.P. Wu, R.Y. Sun, R.H. Chen et al., SEINA: a two-dimensional steam explosion integrated analysis code. Nucl. Eng. Technol. **54**, 3909–3918 (2022). https://doi.org/10.1016/j.net.2022.04.025
4. L. He, P. Liu, X. Zhang et al., Experimental study on the effects of boiling during molten jet and coolant interactions. Ann. Nucl. Energy **143**, 107392 (2020). https://doi.org/10.1016/j.anucene.2020.107392
5. Y. Xiang, D. Liang, A. Komlev et al., An experimental investigation on debris bed formation from fuel coolant interactions of metallic and oxidic melts. Appl. Therm. Eng. **233**, 121186 (2023). https://doi.org/10.1016/j.applthermaleng.2023.121186
6. Y. Deng, Q. Guo, D. Fang et al., A numerical study on the levitation system for droplet preparation in a fuel-coolant interaction experiment. Prog. Nucl. Energ. **159**, 104639 (2023). https://doi.org/10.1016/j.pnucene.2023.104639

7. X. Cao, Y. Tobita, S. Kondo, A thermal fragmentation model induced by surface solidification. J. Nucl. Sci. Technol. **39**, 628–636 (2002). https://doi.org/10.1080/18811248.2002.9715243
8. C. Peng, L. Tong, X. Cao, Preliminary study on the fuel-coolant interaction triggered by thermal effect. Ann. Nucl. Energy. **98**, 112–119 (2016). https://doi.org/10.1016/j.anucene.2016.07.033
9. Q. Lin, L. Tong, X. Cao et al., Vapor film collapse triggered by external pressure pulse and the fragmentation of melt droplet in FCIs. Nucl. Sci. Tech. **19**, 246–250 (2008). https://doi.org/10.1016/S1001-8042(08)60058-5
10. R. Sun, L. Wu, W. Ding et al., From melt jet break-up to debris bed formation: a review of melt evolution model during fuel-coolant interaction. Ann. Nucl. Energy. **165**, 108642 (2022). https://doi.org/10.1016/j.anucene.2021.108642
11. Y. Iwasawa, Y. Abe, Melt jet-breakup and fragmentation phenomena in nuclear reactors: a review of experimental works and solidification effects. Prog. Nucl. Energy. **108**, 188–203 (2018). https://doi.org/10.1016/j.pnucene.2018.05.009
12. M. Johnson, Y. Emura, R. Clavier et al., A mechanism for spontaneous thermal fragmentation with coolant entrainment during the molten fuel-sodium interaction. Nucl. Eng. Des. **423**, 113165 (2024). https://doi.org/10.1016/j.nucengdes.2024.113165
13. S.K. Das, A.K. Sharma, E.H. Rao et al., Post accident heat removal: numerical and experimental simulation. Nucl. Eng. Des. **265**, 1246–1254 (2013). https://doi.org/10.1016/j.nucengdes.2013.09.032
14. E.H. Rao, A.K. Acharya, P.K. Shukla et al., Investigation of molten fuel coolant interaction with simulated corium in sodium. Ann. Nucl. Energy. **206**, 110640 (2024). https://doi.org/10.1016/j.anucene.2024.110640
15. M. Epstein, A. Karahan, J. Liao et al., Models for fuel ejection from a failed annular fuel pin in a lead cooled fast reactor: fuel/coolant interaction and fission gas/fuel jet impingement heating implications. Ann. Nucl. Energy. **181**(109499), 866 (2023). https://doi.org/10.1016/j.anucene.2022.109499
16. G. Li, P. Wen, H. Feng et al., 2D MPS analysis of hydrodynamic fine fragmentation of melt drop with initial steam film during fuel-coolant interaction. Ann. Nucl. Energy. **142**, 107378 (2020). https://doi.org/10.1016/j.anucene.2020.107378
17. G. Li, P. Yao, P. Wen et al., Numerical study of hydraulic fragmentation of melt jet in coolant: breakup length and melt-coolant contact area. Prog. Nucl. Energ. **145**, 104131 (2022). https://doi.org/10.1016/j.pnucene.2022.104131
18. T. Li, Y. Yang, M. Yuan et al., Effects of molten material temperatures and coolant temperatures on vapor explosion. Nucl. Sci. Tech. **18**, 311–315 (2007). https://doi.org/10.1016/S1001-8042(07)60068-2
19. W. Huang, R. Sa, D. Zhou et al., Experimental study on fragmentation behaviors of molten LBE and water contact interface. Nucl. Sci. Tech. **26**, 060601 (2015). https://doi.org/10.13538/j.1001-8042/nst.26.060601
20. T. Li, Y. Yang, M. Yuan et al., Experimental investigation on the bursting of single molten droplet in coolant. Nucl. Sci. Tech. **18**, 376–380 (2007). https://doi.org/10.1016/S1001-8042(08)60012-3
21. T. Li, Y. Yang, X. Li et al., Experimental study of high temperature particle dropping in coolant liquid. Nucl. Sci. Tech. **18**, 252–256 (2007). https://doi.org/10.1016/S1001-8042(07)60056-6
22. Q. Lin, X. Cao, Simulation of the mixing process in FCIs with hydrodynamics fragmentation model. Nucl. Sci. Tech. **18**, 242–246 (2007). https://doi.org/10.1016/S1001-8042(07)60054-2
23. S.B. Cheng, Y.H. Dong, X.L. Chen et al., Experimental study on local fuel-coolant interaction in molten pool with different melts. Ann. Nucl. Energy. **149**, 107760 (2020). https://doi.org/10.1016/j.anucene.2020.107760894
24. H.Y. Choi, H. Chae, E.S. Kim, Numerical simulation on jet breakup in the fuel-coolant interaction using smoothed particle hydrodynamics. Nucl. Eng. Technol. **53**, 3264–3274 (2021). https://doi.org/10.1016/j.net.2021.04.021
25. M. Furuya, K. Matsumura, I. Kinoshita, A linear stability analysis of a vapor film in terms of the triggering of vapor explosions. J. Nucl. Sci. Technol. **39**, 1026–1032 (2002). https://doi.org/10.1080/18811248.2002.9715290
26. D.S. Drumheller, The initiation of melt fragmentation in fuel-coolant interactions. Nucl. Sci. Eng. **72**, 347–356 (1979). https://doi.org/10.13182/NSE79-A20390
27. B. Kim, M.L. Corradini, Modeling of small-scale single droplet fuel/coolant interactions. Nucl. Sci. Eng. **98**, 16–28 (1988). https://doi.org/10.13182/NSE88-A23522
28. D.F. Fletcher, Steam explosion triggering: a review of theoretical and experimental investigations. Nucl. Eng. Des. **155**, 27–36 (1995). https://doi.org/10.1016/0029-5493(94)00865-V
29. R. Meignen, B. Raverdy, S. Picchi et al., The challenge of modeling fuel-coolant interaction: part II-Steam 913 explosion. Nucl. Eng. Des. **280**, 528–541 (2014). https://doi.org/10.1016/j.nucengdes.2014.08.028
30. L.S. Nelson, Steam explosions of single drops of pure and alloyed molten aluminum. Nucl. Eng. Des. **155**, 413–425 (1990). https://doi.org/10.1016/0029-5493(94)00886-4
31. T.A. Dullforce, D.J. Buchanan, R.S. Peckover, Self-triggering of small-scale fuel-coolant interactions: I. Experiments. J. Phys. D Appl. Phys. **9**, 1295 (1976). https://doi.org/10.1088/0022-3727/9/9/006
32. N. Kouraytem, E.Q. Li, S.T. Thoroddsen, Formation of microbeads during vapor explosions of field's metal in water. Phys. Rev. E. **93**, 063108 (2016). https://doi.org/10.1103/PhysRevE.93.063108
33. P. Watts, D. Frost, R. Barbone, Influence of fluid properties on the characteristics of single drop fuel-coolant interactions. In: ANS Proceedings of the 1993 National Heat Transfer Conference (1993)
34. M.L. Corradini, Phenomenological modeling of the triggering phase of small-scale steam explosion experiments. Nucl. Sci. Eng. **78**, 154–170 (1981). https://doi.org/10.13182/NSE81-A20101
35. R.C. Hansson, T.N. Dinh, L. Manickam, A study of the effect of binary oxide materials in a single droplet vapor explosion. Nucl. Eng. Des. **264**, 168–175 (2013). https://doi.org/10.1016/J.NUCENGDES.2013.02.017
36. A. Inoue, S.G. Bankoff, Destabilization of film boiling due to arrival of a pressure shock-Part I: experimental. J. Heat Transf. **103**, 459–464 (1981). https://doi.org/10.1115/1.3244486
37. A. Inoue, S. Aoki, M. Aritomi et al., Study on transient heat transfer of film boiling due to arrival of pressure shock. International Heat Transfer Conference 7 (1982)
38. P. Naylor, M. Patrick, Film boiling destabilization. The University of Exeter (1985)
39. J. Min, W. Ma, G. Zhu et al., An experimental study on steam explosion of a small melt jet falling into a water pool. Nucl. Eng. Des. **391**, 111723 (2022). https://doi.org/10.1016/j.nucengdes.2022.111723
40. C. Peng, Influence of coupled factors on premixing and fragmentation of mild thermal interaction. Ann. Nucl. Energy. **160**, 108394 (2021). https://doi.org/10.1016/J.ANUCENE.2021.108394
41. S.J. Tan, Y.B. Zhong, H. Cheng et al., Experimental investigation on the characteristics of molten lead-bismuth non-eutectic alloy fragmentation in water. Nucl. Sci. Tech. **33**, 115 (2022). https://doi.org/10.1007/s41365-022-01097-9
42. J. Min, G. Zhu, Y. Yuan et al., COMSOL simulation for design of induction heating system in VULCAN facility. Sci. Technol. Nucl. Install. **2021**, 9922503 (2021). https://doi.org/10.1155/2021/9922503
43. J.H. Kim, I.K. Park, B.T. Min et al., Results of the triggered steam explosions from the TROI experiment. Nucl. Technol. **158**, 378–395 (2007). https://doi.org/10.13182/NT07-A3849

44. I. Huhtiniemi, H. Hohmann, D. Magallon, FCI experiments in the corium/water system. Nucl. Eng. Des. **177**, 339–349 (1997). https://doi.org/10.1016/S0029-5493(97)00202-1
45. C. Peng, X.P. Meng, J. Deng et al., Theoretical modeling of the drag reduction influenced by film boiling heat transfer on a spherical body. Int. Commun. Heat Mass. **134**, 106028 (2022). https://doi.org/10.1016/j.icheatmasstransfer.2022.106028
46. X. Cao, Y. Tobita, Drag correlations for a hot particle/droplet with vapor film. J. Nucl. Sci. Technol. **38**, 721–728 (2001). https://doi.org/10.1080/18811248.2001.9715088
47. Y.C. Deng, Q. Guo, Y. Xiang et al., An experimental study on steam explosion of multiple droplets in different chemical solutions. Int. J. Heat. Mass. Tran. **226**, 125477 (2024). https://doi.org/10.1016/j.ijheatmasstransfer.2024.125477